
Future-Guided Learning: A Predictive Approach To Enhance Time-Series Forecasting

Skye Gunasekaran¹, Assel Kembay¹, Hugo Ladret², Rui-Jie Zhu¹,
 Laurent Perrinet², Omid Kavehei³, Jason Eshraghian^{1*}

¹University of California, Santa Cruz, CA, USA

²Friedrich Miescher Institute for Biomedical Research, Basel, Switzerland

³The University of Sydney, Sydney, Australia

Abstract

Accurate time-series forecasting is crucial in various scientific and industrial domains, yet deep learning models often struggle to capture long-term dependencies and adapt to data distribution drifts over time. We introduce Future-Guided Learning, an approach that enhances time-series event forecasting through a dynamic feedback mechanism inspired by predictive coding. Our method involves two models: a detection model that analyzes future data to identify critical events and a forecasting model that predicts these events based on current data. When discrepancies occur between the forecasting and detection models, a more significant update is applied to the forecasting model, effectively minimizing surprise and adapting to shifts in the data distribution by aligning its predictions with actual future outcomes. This feedback loop allows the forecasting model to dynamically adjust its parameters, focusing on persistent features despite changes in the data. We validate our approach on a variety of tasks, demonstrating a 44.8% increase in AUC-ROC for seizure prediction using EEG data, and a 48.7% reduction in MSE for forecasting in nonlinear dynamical systems. By incorporating a predictive feedback mechanism adaptable to data drift, Future-Guided Learning advances how deep learning is applied to time-series forecasting. Our code is publicly available at <https://github.com/SkyeGunasekaran/FutureGuidedLearning>.

1 Introduction

Time-series forecasting is a well-researched area in statistics and machine learning, with wide applicability in financial markets, weather prediction, and biomedical signal analysis. In recent years, deep learning models have been increasingly applied to time-series forecasting, leveraging their ability to model complex, nonlinear relationships within data [17].

Despite these advancements, challenges remain in accurately capturing long-term dependencies due to inherent stochasticity and noise in signals. Time-series data involve complex temporal dynamics and often exhibit non-stationary behaviors. Additionally, they are frequently subject to external influences and perturbations which introduce abrupt changes in the data patterns, making long-term forecasting difficult. As a result, even advanced deep learning models, such as Transformer-based time-series foundation models, face difficulties when tasked with long-term predictions [14, 5].

To address these challenges, we introduce Future-Guided Learning (FGL), an approach that draws on predictive coding and employs a dynamic feedback mechanism to enhance time-series event forecasting. By leveraging a future-oriented detection model that guides a past-oriented forecasting

*Corresponding author, email to: jsn@ucsc.edu

model, FGL introduces a temporal interplay reminiscent of Knowledge Distillation (KD) [10], where a “teacher” can provide insights that improve a “student” model’s long-horizon predictions.

Importantly, FGL is rooted in the theory of predictive coding, which views the brain as an inference machine continuously refining its internal models based on discrepancies, known as “prediction errors” [30, 7, 25, 15], between expected and actual observations. This process is inherently temporal, as it involves updating predictions over time to minimize error and refine future estimates. In its hierarchical form, predictive coding posits that neurobiological networks compute these errors across different levels of abstraction, progressively building internal models of the world [21, 26].

Despite its potential to model spatio-temporal information, predictive coding’s impact on modern deep learning has been limited [18, 8]. Prior research has explored its use as a biologically plausible alternative to gradient descent [19, 6] and applied it in hierarchical recurrent networks for supervised and unsupervised learning tasks [29, 26]. While predictive coding has been employed in time-series forecasting, integrating it with modern deep learning methods to achieve state-of-the-art performance remains a significant challenge.

In this work, we validate FGL across two distinct domains: biomedical signal analysis and time-series forecasting of dynamical systems. In the biomedical domain, we focus on seizure prediction using EEG data, where results show an average increase of 44.8% in AUC-ROC across patients. In the dynamical systems domain, we demonstrate FGL’s benefits using the Mackey-Glass equation, where a 48.7% decrease in mean squared error (MSE) is observed. These results demonstrate that FGL not only improves forecasting accuracy but also introduces a robust method for utilizing uncertainty across time horizons, thus naturally connecting to predictive coding theory.

2 Methodology

Traditional KD involves transferring probabilistic class information between two models that share the same representation space. In our approach, we reformulate this student-teacher dynamic by placing the teacher model in the relative future of the student model, introducing a temporal difference in the representation space between them.

Our distillation method follows that of Hinton et al. [10], where the student model is trained using a combination of the cross-entropy loss with the ground truth labels and the Kullback-Leibler (KL) divergence between the softmax outputs of the student and teacher models. This dual objective allows the student to learn from both the true data and the future-oriented predictions of the teacher.

$$\mathcal{L} = \underbrace{\alpha \times - \sum Y_{\text{true}} \cdot \sigma(\text{logits}_{S,t})}_{\text{Cross-Entropy Loss}} + (1 - \alpha) \times \underbrace{\sum \sigma(\text{logits}_{T,t+n}) \cdot \left[\log \left(\frac{\sigma(\text{logits}_{T,t+n})}{\sigma(\text{logits}_{S,t})} \right) \right]}_{\text{Time-Offset KL Divergence Loss}} \quad (1)$$

Here, α is a hyperparameter that balances the contributions of the cross-entropy and KL divergence components of the loss function, and are summed over logits. Crucially, the logits of the teacher (T) and student (S) are offset in time: the teacher’s logits in the numerator and the student’s logits in the denominator correspond to different time steps within the sequence, offset by n time steps.

For instance, given a time-series biomedical signal (e.g., EEG) X_t sampled at time t , the student model S aims to forecast whether a seizure will occur n steps into the future (i.e., at time $t + n$). The teacher model T determines whether a seizure is currently occurring at time $t + n$ using data X_{t+n} . An illustration of this time offset is provided in Figure 1(b).

The KL divergence term measures the difference between the probability distributions of the student and teacher models, effectively distilling the “uncertainty” of the teacher into the student. Unlike traditional KD, our approach leverages a temporal offset between the student and teacher models. At any given student time step t , the teacher model provides logits from a future time step $t + n$. This temporal difference allows the student to learn from the teacher’s future-oriented knowledge, capturing time-variant patterns and uncertainties that are not accessible from the student’s current time step alone. By incorporating this offset, the distillation process helps the student model learn richer spatial and temporal information, enhancing its forecasting capabilities.

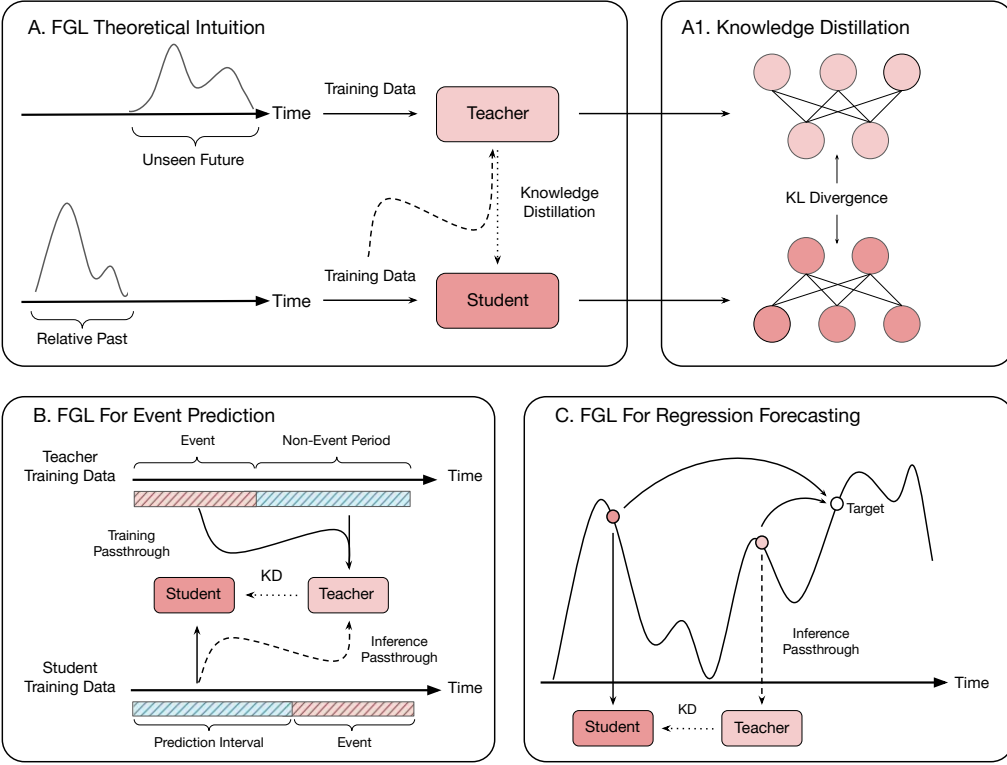


Figure 1: (A) In the FGL framework, a teacher model operates in the relative future of a student model that focuses on long-term forecasting. After training the teacher on its future-oriented task, both models perform inference during the student’s training phase. The probability distributions from the teacher and student are extracted, and a loss is computed based on Equation 1. (A1) Knowledge distillation transfers information via the Kullback-Leibler (KL) divergence between class distributions. (B) In an event prediction setting, the teacher is trained directly on the events themselves, while the student is trained to forecast these events. Future labels are distilled from the teacher to the student, guiding the student to align more closely with the teacher model’s predictions, despite using data from the relative past. (C) In a regression forecasting scenario, the teacher and student perform short-term and long-term forecasting, respectively. Similar to event prediction, the student gains insights from the teacher during training, enhancing its ability to predict further into the future.

3 Future-Guided Learning For Event Prediction

Seizure forecasting provides an ideal test case for evaluating FGL, as it requires both detecting seizures and predicting their onset in advance. More specifically, a seizure detection model can offer valuable insights to a seizure forecasting model, which does not explicitly learn the characteristics of a seizure but must still accurately anticipate its occurrence.

For the task of seizure forecasting, we utilize two primary datasets: the Children’s Hospital Boston MIT (CHBMIT) dataset [23] and the American Epilepsy Society Seizure Prediction Challenge (AES) dataset [4]. Further details on dataset characteristics and preprocessing steps can be found in Appendix A.1 and A.2, respectively.

3.1 CHBMIT: Patient Specific FGL

On the CHBMIT dataset, FGL was performed by first pre-training a unique teacher model for seizure detection on each patient for 50 epochs. During this pre-training phase, preictal segments were excluded, as their inclusion would reduce the uncertainty we aim to distill during the student training phase. Next, during the training of the student model over 25 epochs, each data point was fed into both the student and teacher models, and the corresponding class probabilities were obtained. The

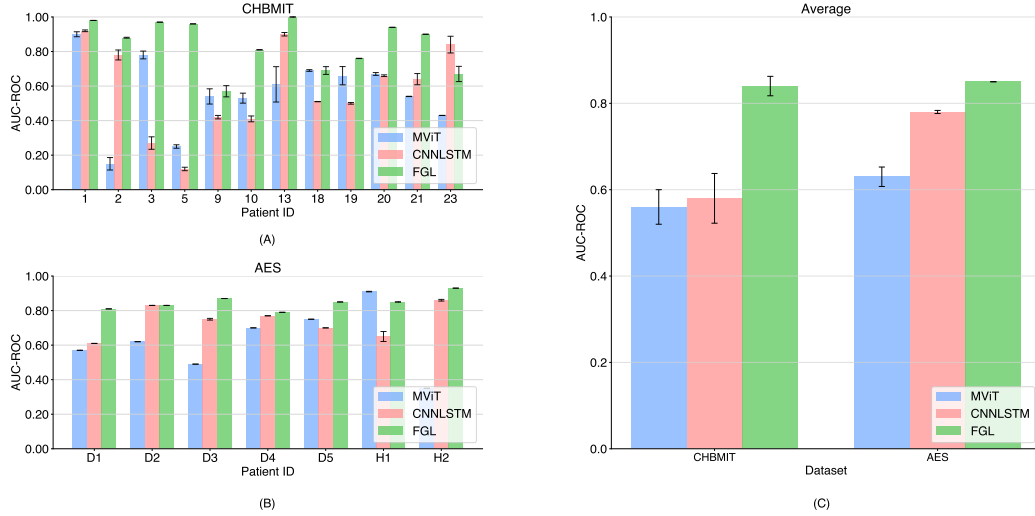


Figure 2: Seizure Prediction results on (a) CHBMIT and (b) AES datasets. Three methods are tested: an MViT, a CNN-LSTM, and FGL. All results were calculated over 3 continuous trials. The means and variance bars are reported.

loss function defined in Equation (1) was then used to compute the student model’s loss. A range of α values was tested to balance the contributions of the cross-entropy and KL divergence components of the loss function. The optimal α for each patient was selected based on a hyperparameter sweep, with detailed results presented in Appendix A.2 Fig. 6. Different values of α were tested to balance the cross-entropy and KL divergence components of the loss, with the optimal value selected through a hyperparameter sweep for each patient. The temperature parameter for the KD loss was fixed at $T = 4$. We used the SGD optimizer with a learning rate of 5×10^{-4} . Both the student and teacher models were implemented as CNN-LSTM architectures.

3.2 AES: Patient Non-Specific FGL

When future data from the same distribution as the student model is unavailable, it is still possible to train a teacher model using future data from an out-of-distribution source. We test this approach on the AES dataset, which contains only preictal samples without any labeled seizures. Due to the lack of corresponding seizure data, we use a separate dataset: the UPenn and Mayo Clinic seizure dataset [13] to create the teacher model.

The AES dataset comprises recordings from 5 dogs and 2 humans, while the UPenn and Mayo Clinic dataset includes 4 dogs and 8 human patients. Given this discrepancy, we constructed two “universal teachers” from the latter dataset: one based on dog seizures and the other on human seizures. These universal teacher models were trained using a combined set of interictal data from selected patients, interspersed with randomly sampled seizures from a diverse pool of patients. This approach allows the teacher model to learn generalized seizure features from a wide variety of cases.

A challenge in using different data sources for the teacher model was the inconsistency in data characteristics and formats between datasets. We addressed this issue by selecting the top k most significant EEG channels for each teacher model based on their contribution to seizure detection scores [27]. The number of selected channels was then adjusted based on the requirements of each student model, ensuring compatibility and effective knowledge transfer. As with the CHBMIT dataset, an ablation study of the influence of α is provided in Appendix A.2 Fig. 7.

3.3 Event Prediction Results

To compare our method with state-of-the-art (SOTA) approaches, we tested FGL against a Multi-Channel Vision Transformer (MViT) [11] and a CNN-LSTM [22, 31]. These models are commonly

used in medical settings for temporal data and have demonstrated strong efficacy. Further details, including results on false positive rate (FPR) and sensitivity, are provided in Appendix A.3.

On the CHBMIT dataset, our results show a significant improvement with FGL compared to the baseline, with an average 44.8% increase in the area under the receiver operating characteristic curve (AUC-ROC), as shown in Fig. 2(a-c). Additionally, FGL enhanced predictions across most patients, with the largest gain observed for patient 5 by a factor of $3.84\times$. The performance dropped only for patient 23 by a factor of $0.80\times$ compared to the CNN-LSTM, but still significantly outperformed the MViT architecture.

On the AES dataset, where the teacher model was trained on a different set of seizure patients and then used on new individuals at test time, FGL still achieved an average performance improvement of 8.9% over the CNN-LSTM, as shown in Fig. 2(b). Further details on implementation and preprocessing are provided in Section 3 and Appendix A.2, respectively.

3.4 Event Prediction Discussion

Our results on both the CHBMIT and AES datasets show a remarkable improvement in predictive accuracy when using FGL. The small number of seizures per patient lead to a considerable variance in performance across patients, though in all test cases, FGL reduced this variance as can be seen by the error bars in Fig. 2(c).

FGL is sensitive to the performance of the teacher model. Unlike the CHBMIT dataset, which used patient-specific teacher models, FGL on AES used a teacher model trained across all patients. This introduces a trade-off: a teacher model that is tuned to an individual patient’s epileptic signature vs. having access to more samples to train a universal teacher model [9]. While the patient-specific teacher resulted in the larger boost in AUC-ROC, it came with considerable variance. Patients 5, 10, 20 and 21 showed a significant boost in performance while most other patients had small improvements. For the universal teacher in AES, the improvements were more modest, but also more consistent.

4 Future-Guided Learning For Regression Forecasting

Regression is used to model continuous, nonlinear relationships in time-series data, especially when capturing complex temporal patterns is the focus rather than classifying discrete events. Traditional regression methods often struggle with chaotic signals, where small changes can cause large deviations in predictions, highlighting the need for more robust techniques.

To test our approach, we use the Mackey-Glass (MG) delay differential equation, a standard model for generating chaotic time-series data. Originally developed for blood cell regulation, the MG equation is widely used as a benchmark due to its highly non-linear and unpredictable behavior. Details of the equation and parameter settings are provided in Appendix B.1.

Standard regression tasks typically minimize mean squared error (MSE), but this objective does not capture model uncertainty, treating predictions as fixed point estimates. This limitation underscores the need for methods that account for uncertainty, particularly with chaotic time-series data like those produced by the MG equation.

4.1 Regression Forecasting Implementation

To address the challenge of regression uncertainty, we discretize the target values into “bins”, as illustrated in Figure 4(a). The number of bins determines the number of output neurons in the network, with each bin treated as a separate class. Increasing the number of bins reduces the margin for error in the network’s predictions, making the forecasting task more challenging. However, it allows for a finer-grained representation of the output as a probability distribution across bins.

In addition, we reformulate the tasks of the teacher and student models to better align with regression objectives. The teacher model performs next-step forecasting, while the student model focuses on longer-term predictions. This difference in forecasting horizons explicitly enforces a variance in timescales between the models. More specifically, given an input sample at x_t , the student model

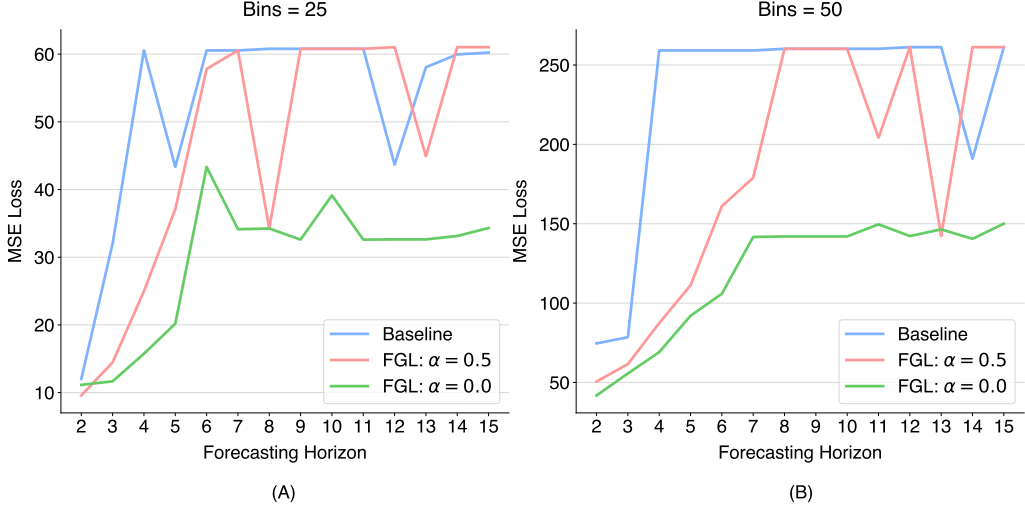


Figure 3: Mackey Glass forecasting results with (A) 25 and (B) 50 bins. Results show the MSE loss at each horizon. $\alpha = 0$ indicates where the student is trained using the distilled label only, and $\alpha = 0.5$ is where a mix of both the distilled and ground truth label are used. A table of results is available in Appendix C.

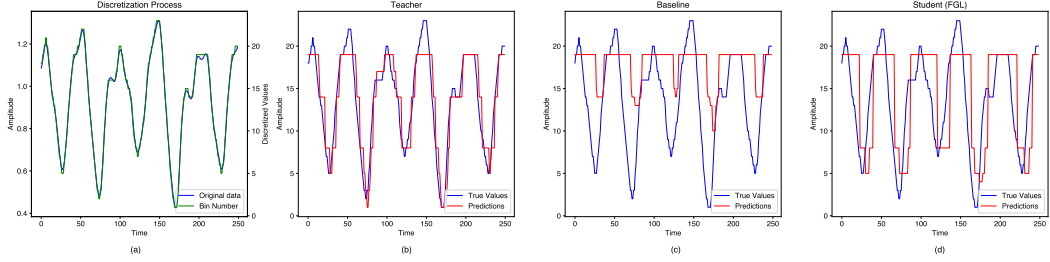


Figure 4: (a) Discretization Process of Mackey Glass. After data generation, each target value X_{t+n} is assigned to a discrete value based on the number of bins and the range of data. Moreover, the number of output neurons matches the number of bins, such that each bin is treated as a separate class label. (b) Teacher model performs next-step prediction, (c) Student model with FGL forecasts $n = 5$ steps into the future, (d) Baseline student model prediction without FGL, also forecasting 5 steps into the future. FGL allows the student model to capture neighboring spatial information of the target, leading to lower MSE loss and richer representation.

aims to predict n steps into the future, targeting x_{t+n} . In contrast, the teacher model is tasked with predicting the immediate next step and is provided with the input data at x_{t+n-1} .

Similar to event prediction, the teacher model is pretrained first, followed by inference within the student training loop, where the loss defined in Equation (1) is computed. During model testing, we select the neuron with the highest probability and compute the corresponding MSE, aligning this approach with traditional regression evaluation methods.

We compare two scenarios: $\alpha = 0.5$ and $\alpha = 0.0$, to assess the effect of using only the teacher's uncertainty versus combining it with the ground truth labels. For our experiments, we employed a single-layer recurrent neural network (RNN), used a batch size of 1, and trained the teacher model for 20 epochs, while both the student and baseline models were trained for 15 epochs.

4.2 Regression Forecasting Results

The results show that FGL consistently outperforms the baseline models, achieving an average reduction of 46.4% in MSE with 25 bins, and 48.7% reduction with 50 bins. This improvement is particularly pronounced at $\alpha = 0$, where the ground truth labels are completely excluded, and

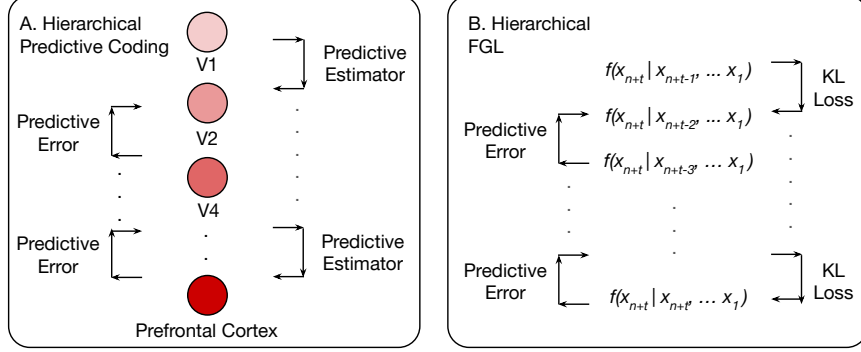


Figure 5: (A) Illustration of predictive coding in the brain. Information is received by the primary visual cortex (V1), which then propagates to different areas of the brain with more complex levels of abstraction. This propagation takes the form as a predictive estimator: higher level areas aid in prediction of lower level areas. The difference between the prediction and true output is the predictive error. Areas with lighter colors represent low-level abstractions, where darker colors represent the increasing representational demand (thoughts, movement, etc). (B) Hierarchical FGL propagates information via uncertainty, in other words, FGL substitutes the predictive estimator with the uncertainty of each layer. This uncertainty is conveyed via the KL divergence of between each layer’s probability distribution with the successive layer. The difference between each layer’s prediction and true output is the predictive error. In both models, areas lower in the hierarchy process information in a delayed manner, as they are the last to receive it. As the demand for complexity increases, so does the predictive error.

training relies entirely on knowledge distillation from the teacher model. As the forecasting horizon extends, it is expected that the MSE for all cases will increase, but we found that the rate of increase of FGL is slower than that of the baseline. This indicates that FGL exhibits a stronger tolerance to a varying forecasting horizon.

When $\alpha = 0$, FGL exhibits the slowest increase in MSE across forecasting horizons. This behavior can be attributed to the student model’s strong reliance on the teacher’s future-oriented knowledge, which helps stabilize the predictions over longer time frames. In contrast, at $\alpha = 0.5$, the MSE increases faster than at $\alpha = 0$, but still grows at a slower rate compared to the baseline. Here, the partial use of ground truth labels introduces some variability, but the distillation from the teacher continues to provide a stabilizing effect. Eventually, the MSE at $\alpha = 0.5$ approaches that of the baseline, indicating a saturation point where the benefits of distillation diminish. Critically, FGL improves performance over the baseline in almost all cases.

4.3 Regression Forecasting Discussion

When compared to the baseline method, FGL improved MSE loss across all forecasting horizons, with the most pronounced gains observed at longer horizons. This trend can be attributed to the nature of the forecasting task: shorter-term predictions inherently have lower error due to their temporal proximity, leaving less room for improvement. In contrast, long-term forecasting is more challenging due to increased uncertainty and error accumulation. Here, the information transferred from the future-oriented teacher model plays a greater role in guiding the student model, helping it make more accurate predictions and mitigate the error growth typical at extended horizons.

A limitation in our regression forecasting formulation is the discretization process (Fig. 4), which can reduce the precision of the model’s predictions. While discretization aids in estimating uncertainty, it also imposes artificial boundaries on the prediction space, potentially limiting the model’s ability to make fine-grained forecasts. To better align with traditional time-series forecasting methods, future work should investigate alternative approaches for uncertainty quantification that avoid the need for discretization.

5 Future-Guided Learning And Predictive Coding

The teacher and student models can be described more precisely using a Bayesian prediction framework. Consider a network $f(x_{t+n}|x_{t+n-1}, \dots, x_1)$, whose objective is to predict the next step x_{t+n} given the preceding sequence x_{t+n-1}, \dots, x_1 . The state of the network up to this point can be expressed as the product of the likelihood $f(x|\theta)$ and the current posterior distribution $\pi(\theta|x_1, \dots, x_{t+n-1})$. In essence, the network generates predictions by integrating information accumulated up to the current time step.

$$\text{teacher} = f(x_{t+n}|x_{t+n-1}, x_{t+n-2}, \dots, x_1) = \sum f(x_{t+n}|\theta) \cdot \pi(\theta|x_1, \dots, x_{t+n-1}) \quad (2)$$

$$\text{student} = f(x_{t+n}|x_t, x_{t-1}, \dots, x_1) = \sum f(x_t|\theta) \cdot \pi(\theta|x_1, \dots, x_t) \quad (3)$$

The teacher model has access to data beyond the current time step, leveraging x_{t+n-1}, \dots, x_1 , while the student model is constrained to information available up to x_t . The divergence between the teacher and student models can be quantified using the KL divergence, which measures how the student's predictions deviate from the teacher's more informed predictions:

$$D_{KL}(\text{teacher} \parallel \text{student}) = \sum f(x_{t+n}|x_{t+n-1}, \dots, x_1) \cdot \log\left(\frac{f(x_{t+n}|x_{t+n-1}, \dots, x_1)}{f(x_{t+n}|x_t, \dots, x_1)}\right) \quad (4)$$

The intuition behind the KL divergence lies in quantifying the difference between the predictive distributions of the teacher and student models. When forecasting future events, the student model is inherently less informed than the teacher model, as the teacher has access to an additional $n - 1$ time points beyond the student's observational window. This additional information enables the teacher to construct a more accurate predictive distribution. The KL divergence, therefore, represents the “well-informedness” of the teacher model relative to the student model. As the forecasting horizon increases, the representational complexity for the student grows, as it must account for higher levels of uncertainty and potential chaos in the data.

To address this challenge, we extend the student-teacher framework across a temporal hierarchy, linking models operating at different time steps. The topmost model, associated with the current time step x_{n+t-1} , acts as a teacher to the model at x_{n+t-2} , which in turn is another teacher to the model at x_{n+t-3} , and so on. This relationship propagates downwards, with each model at time step x_{n+t-k} serving as a teacher to the subsequent model at $x_{n+t-(k+1)}$, ultimately connecting to the bottommost model at x_t . Instead of distilling knowledge directly from the topmost model to the bottommost model, we propose a chained uncertainty propagation through these intermediate models. Each model in the hierarchy operates on a distinct timescale, resulting in temporally stratified representations that progressively refine the forecasting process at varying levels of granularity.

This approach bears similarity to a potential implementation of hierarchical predictive coding in the brain. Low-level cortical areas, such as the primary visual cortex (V1), function analogously to the intermediate models in hierarchical FGL, as they process detailed sensory inputs over short timescales (e.g., $f(x_{n+t}|x_{n+t-1}, \dots, x_t)$). In contrast, higher-level cortical areas like the prefrontal cortex correspond to the bottommost student model, $f(x_{n+t}|x_n, \dots, x_t)$, as they integrate abstract patterns and process temporally delayed information over longer timescales. A visual representation of this hierarchical structure is provided in Figure 5.

From a practical standpoint, treating the teacher model as a true Bayesian posterior is often unrealistic, as the posterior distribution is typically intractable. One solution is to use variational inference, where the network optimizes the parameters of a surrogate distribution to approximate the posterior [18, 3]. In this framework, we conceptualize the teacher model as a well-posed surrogate distribution, $T \approx q(v)$, and the student model as a prior distribution, $S = p(v)$. When the teacher closely approximates the true posterior, the difference in loss between the student and teacher provides meaningful feedback to the student model. This difference can be quantified using a metric such as KL divergence:

$$\begin{aligned}
D_{\text{KL}}(q(v) \parallel p(v|u)) &= \int q(v) \ln \frac{q(v)}{p(v|u)} dv \\
&= \int q(v) \ln \frac{q(v)}{p(u, v)} dv + \ln p(u)
\end{aligned} \tag{5}$$

The first term on the right-hand side is known as the free energy, F [18], allowing us to rewrite this variational inference procedure as:

$$\ln p(u) = -F + D_{\text{KL}}(q(v) \parallel p(v|u)). \tag{6}$$

Here, $\ln p(u)$ represents the “surprise” of the student model, directly related to its uncertainty. Since the KL divergence is non-negative, F serves as a lower bound for the surprise $\ln p(u)$. Therefore, maximizing F is equivalent to minimizing the surprise $\ln p(u)$, improving the approximation of the surrogate distribution $q(v)$.

To model the transfer of information between the teacher and student models, we incorporate uncertainty into predictive errors. This relationship can be expressed as:

$$\ln p(u) \approx \frac{1}{2} \left[-\ln \Sigma_p - \frac{(\Phi - v_p)^2}{\Sigma_p} - \ln \Sigma_u - \frac{(u - g(\Phi))^2}{\Sigma_u} \right], \tag{7}$$

where Σ_p and Σ_u represent the predictive variances of the student and teacher models, respectively, v_p is the predicted value of the student, Φ is the teacher’s output, and $g(\Phi)$ denotes a transformation of the teacher’s prediction. These dynamics drive the system toward internal representations that minimize predictive errors, as detailed in Appendix C.

6 Conclusion

We proposed FGL, a novel approach for time-series forecasting and event prediction that leverages temporal variance. By employing a future-oriented teacher model to guide a past-oriented student model, FGL achieved significant improvements: a 44.8% increase in AUC-ROC for biomedical signal analysis and a 48.7% reduction in MSE for time-series forecasting.

While effective, our method has room for improvement, particularly in terms of efficiency and generalization. Training a separate future model can be energy-intensive. A more efficient solution could involve a single model operating across multiple time horizons, where short-term predictions refine longer-term ones. Additionally, task-agnostic techniques like weight comparisons could enhance the adaptability of FGL across various architectures.

Beyond Knowledge Distillation, alternative strategies for leveraging temporal variance could include exploiting moving averages, seasonal trends, or local spatial features. Exploring uncertainty quantification methods that avoid discretization, such as Bayesian inference or Monte Carlo Dropout, may further enhance predictive performance. Overall, our results show the potential of using future-guidance to advance forecasting and event prediction, paving the way for more adaptive and robust methods in time-series analysis.

References

- [1] Abbasi, B., Goldenholz, D.M.: Machine learning applications in epilepsy. *Epilepsia* **60**(10), 2037–2047 (2019)
- [2] Beghi, E., Giussani, G., Nichols, E., Abd-Allah, F., Abdela, J., Abdelalim, A., Abraha, H.N., Adib, M.G., Agrawal, S., Alahdab, F., et al.: Global, regional, and national burden of epilepsy, 1990–2016: a systematic analysis for the global burden of disease study 2016. *The Lancet Neurology* **18**(4), 357–375 (2019)
- [3] Bogacz, R.: A tutorial on the free-energy framework for modelling perception and learning. *Journal of mathematical psychology* **76**, 198–211 (2017)

[4] Brinkmann, B.H., Wagenaar, J., Abbot, D., Adkins, P., Bosshard, S.C., Chen, M., Tieng, Q.M., He, J., Muñoz-Almaraz, F., Botella-Rocamora, P., et al.: Crowdsourcing reproducible seizure forecasting in human and canine epilepsy. *Brain* **139**(6), 1713–1722 (2016)

[5] Das, A., Kong, W., Sen, R., Zhou, Y.: A decoder-only foundation model for time-series forecasting. arXiv preprint arXiv:2310.10688 (2023)

[6] Eshraghian, J.K., Ward, M., Neftci, E.O., Wang, X., Lenz, G., Dwivedi, G., Bennamoun, M., Jeong, D.S., Lu, W.D.: Training spiking neural networks using lessons from deep learning. *Proceedings of the IEEE* (2023)

[7] Friston, K.: A theory of cortical responses. *Philosophical transactions of the Royal Society B: Biological sciences* **360**(1456), 815–836 (2005)

[8] Friston, K.: Does predictive coding have a future? *Nature neuroscience* **21**(8), 1019–1021 (2018)

[9] Herbozo Contreras, L.F., Truong, N.D., Eshraghian, J.K., Xu, Z., Huang, Z., Bersani-Veroni, T.V., Aguilar, I., Leung, W.H., Nikpour, A., Kavehei, O.: Neuromorphic neuromodulation: Towards the next generation of closed-loop neurostimulation. *PNAS nexus* **3**(11), pgae488 (2024)

[10] Hinton, G., Vinyals, O., Dean, J.: Distilling the knowledge in a neural network. arXiv preprint arXiv:1503.02531 (2015)

[11] Hussein, R., Lee, S., Ward, R.: Multi-channel vision transformer for epileptic seizure prediction. *Biomedicines* **10**(7), 1551 (2022)

[12] Jasper, H.H.: Ten-twenty electrode system of the international federation. *Electroencephalogr Clin Neurophysiol* **10**, 371–375 (1958)

[13] Kaggle: Upenn and mayo clinic's seizure detection challenge. <https://www.kaggle.com/c/seizure-detection> (2014)

[14] Ke, Y., Liang, Y., Shi, Z., Song, Z., Yang, C.: Curse of attention: A kernel-based perspective for why transformers fail to generalize on time series forecasting and beyond. arXiv preprint arXiv:2412.06061 (2024)

[15] Keller, G.B., Mrsic-Flogel, T.D.: Predictive processing: a canonical cortical computation. *Neuron* **100**(2), 424–435 (2018)

[16] Kuhlmann, L., Lehnertz, K., Richardson, M.P., Schelter, B., Zaveri, H.P.: Seizure prediction—ready for a new era. *Nature Reviews Neurology* **14**(10), 618–630 (2018)

[17] Lai, G., Chang, W.C., Yang, Y., Liu, H.: Modeling long-and short-term temporal patterns with deep neural networks. In: The 41st international ACM SIGIR conference on research & development in information retrieval. pp. 95–104 (2018)

[18] Millidge, B., Seth, A., Buckley, C.L.: Predictive coding: a theoretical and experimental review. arXiv preprint arXiv:2107.12979 (2021)

[19] Millidge, B., Tschantz, A., Buckley, C.L.: Predictive coding approximates backprop along arbitrary computation graphs. *Neural Computation* **34**(6), 1329–1368 (2022)

[20] Murphy, K.P.: Machine learning: a probabilistic perspective. MIT press (2012)

[21] Rao, R.P., Ballard, D.H.: Predictive coding in the visual cortex: a functional interpretation of some extra-classical receptive-field effects. *Nature neuroscience* **2**(1), 79–87 (1999)

[22] Shahbazi, M., Aghajan, H.: A generalizable model for seizure prediction based on deep learning using cnn-lstm architecture. In: 2018 IEEE Global Conference on Signal and Information Processing (GlobalSIP). pp. 469–473. IEEE (2018)

[23] Shoeb, A.H., Guttag, J.V.: Application of machine learning to epileptic seizure detection. In: Proceedings of the 27th international conference on machine learning (ICML-10). pp. 975–982 (2010)

[24] Siddiqui, M.K., Morales-Menendez, R., Huang, X., Hussain, N.: A review of epileptic seizure detection using machine learning classifiers. *Brain informatics* **7**(1), 5 (2020)

[25] Spratling, M.W.: Predictive coding as a model of response properties in cortical area v1. *Journal of neuroscience* **30**(9), 3531–3543 (2010)

- [26] Spratling, M.W.: A hierarchical predictive coding model of object recognition in natural images. *Cognitive computation* **9**(2), 151–167 (2017)
- [27] Truong, N.D., Kuhlmann, L., Bonyadi, M.R., Yang, J., Faulks, A., Kavehei, O.: Supervised learning in automatic channel selection for epileptic seizure detection. *Expert Systems with Applications* **86**, 199–207 (2017)
- [28] Truong, N.D., Nguyen, A.D., Kuhlmann, L., Bonyadi, M.R., Yang, J., Ippolito, S., Kavehei, O.: Convolutional neural networks for seizure prediction using intracranial and scalp electroencephalogram. *Neural Networks* **105**, 104–111 (2018)
- [29] Tschantz, A., Millidge, B., Seth, A.K., Buckley, C.L.: Hybrid predictive coding: Inferring, fast and slow. *PLoS Computational Biology* **19**(8), e1011280 (2023)
- [30] Von Helmholtz, H.: *Handbuch der physiologischen Optik*, vol. 9. Voss (1867)
- [31] Yang, Y., Truong, N.D., Eshraghian, J.K., Nikpour, A., Kavehei, O.: Weak self-supervised learning for seizure forecasting: a feasibility study. *Royal Society Open Science* **9**(8), 220374 (2022)

A Additional Seizure Information

A.1 Epilepsy Background Information

Epilepsy is a neurological condition which affects millions of people worldwide. It is characterized by a rapid firing in brain activity, often leading to spasms and involuntary muscle movements. Events of epilepsy are referred to as “ictal” events, whereas pre-seizure and non-seizure periods are referred to as “preictal” and “interictal”, respectively [2].

Due to the unpredictable nature of seizures, there has been a widespread effort for decades to create accurate seizure prediction mechanisms [1, 24]. However, attempts to do so have faced many challenges due to patient specificity, high noise of signals, and sparseness of seizure events. To further complicate the task, there has been contradicting evidence regarding the relationship between preictal and ictal events [16].

Patients with epilepsy who are undergoing medical treatment are typically monitored via scalp EEG, in which a varying number of nodes are placed on the patients head according to the 10-20 international standard [12]. Clinicians are tasked with monitoring these signals actively, and can sound an alarm when a seizure takes place to alert medical staff. Therefore, having an accurate seizure forecasting mechanism can help alleviate this burden on hospitals [16].

A.2 Seizure Data Preprocessing

Our prepossessing pipeline of EEG data is as follows. Patient data is classified into three separate categories: interictal, preictal, and ictal. With respect to preictal data, we use a seizure occurrence period of 30 minutes, and a seizure prediction horizon of 5 minutes. Data up to 5 minutes prior to seizure onset is concealed from the student, and the 30 minutes prior to this is labeled as preictal data [28]. Due to this restriction, patients whose preictal data was not long enough were omitted from the dataset.

Each data sample undergoes a short-time-fourier transform (STFT) with a window size of 30 seconds. On both preictal and ictal data, we apply oversampling by taking a sliding window of STFTs. These overlapping samples are removed in the testing set. Our train-test-split was created by concatenating all of the interictal data, and evenly distributing them between ictal or preictal periods. The final 35% of seizures, as well as their corresponding interictal data, are used for testing. No shuffling is performed to preserve the temporal order of data.

Our model of choice for both datasets was a CNN-LSTM. We used two sets of Conv3d layers, an LSTM with three hidden layers, and two linear layers. All models were trained using an NVIDIA RTX 4080 GPU.

A.3 Experimental Details and SOTA Comparison

We conducted an ablation study on FGL by sweeping the hyperparameter α from Equation 1, which balances the cross-entropy and time-offset KL divergence losses, in increments of 0.1. A smaller α increases the KL divergence component while reducing the cross-entropy component. For each patient, the optimal α was identified, and sensitivity, false positive rate (FPR), and AUC-ROC were computed across three trials. Experiments used a softmax temperature of 4 and the SGD optimizer with a learning rate of 5×10^{-4} and momentum of 0.9. Sensitivity and FPR thresholds were determined using Youden’s J statistic, with the best scores for each patient highlighted in **bold**.

Table 1: CHBMIT Comparison with SOTA

Patient	MViT			CNNLSTM			FGL		
	FPR	Sensitivity	AUCROC	FPR	Sensitivity	AUCROC	FPR	Sensitivity	AUCROC
1	0.02 \pm 0.02	0.82 \pm 0.22	0.90 \pm 0.12	0.11 \pm 0.12	0.88 \pm 0.10	0.92 \pm 0.07	0.04 \pm 0.01	0.89 \pm 0.04	0.98 \pm 0.01
2	0.63 \pm 0.45	0.66 \pm 0.47	0.15 \pm 0.19	0.35 \pm 0.33	0.89 \pm 0.15	0.78 \pm 0.17	0.10 \pm 0.04	0.83 \pm 0.18	0.88 \pm 0.05
3	0.16 \pm 0.04	0.66 \pm 0.23	0.78 \pm 0.15	0.42 \pm 0.40	0.49 \pm 0.41	0.27 \pm 0.19	0.01 \pm 0.01	0.90 \pm 0.02	0.97 \pm 0.01
5	0.61 \pm 0.43	0.66 \pm 0.47	0.25 \pm 0.10	0.65 \pm 0.46	0.67 \pm 0.47	0.12 \pm 0.10	0.07 \pm 0.00	0.97 \pm 0.01	0.96 \pm 0.01
9	0.20 \pm 0.16	0.41 \pm 0.41	0.54 \pm 0.21	0.64 \pm 0.45	0.67 \pm 0.47	0.42 \pm 0.10	0.60 \pm 0.04	0.94 \pm 0.02	0.57 \pm 0.18
10	0.25 \pm 0.17	0.48 \pm 0.13	0.53 \pm 0.17	0.56 \pm 0.38	0.61 \pm 0.34	0.41 \pm 0.13	0.26 \pm 0.04	0.65 \pm 0.07	0.81 \pm 0.03
13	0.18 \pm 0.14	0.67 \pm 0.36	0.61 \pm 0.32	0.11 \pm 0.10	0.99 \pm 0.01	0.90 \pm 0.10	0.00 \pm 0.00	0.99 \pm 0.01	1.00 \pm 0.00
18	0.30 \pm 0.10	0.68 \pm 0.15	0.69 \pm 0.07	0.54 \pm 0.28	0.64 \pm 0.26	0.51 \pm 0.03	0.43 \pm 0.14	0.88 \pm 0.06	0.69 \pm 0.15
19	0.07 \pm 0.05	0.47 \pm 0.33	0.66 \pm 0.23	0.80 \pm 0.04	0.97 \pm 0.01	0.50 \pm 0.07	0.48 \pm 0.10	0.89 \pm 0.07	0.76 \pm 0.03
20	0.38 \pm 0.07	0.98 \pm 0.03	0.67 \pm 0.09	0.45 \pm 0.03	0.95 \pm 0.06	0.66 \pm 0.07	0.13 \pm 0.03	0.86 \pm 0.02	0.94 \pm 0.01
21	0.60 \pm 0.03	1.00 \pm 0.00	0.54 \pm 0.03	0.49 \pm 0.14	0.97 \pm 0.02	0.64 \pm 0.18	0.12 \pm 0.02	0.73 \pm 0.04	0.90 \pm 0.02
23	0.62 \pm 0.06	1.00 \pm 0.00	0.43 \pm 0.02	0.20 \pm 0.27	0.92 \pm 0.12	0.84 \pm 0.22	0.50 \pm 0.08	1.00 \pm 0.00	0.67 \pm 0.21
AVG	0.33 \pm 0.21	0.70 \pm 0.19	0.56 \pm 0.20	0.44 \pm 0.20	0.80 \pm 0.16	0.58 \pm 0.24	0.22 \pm 0.01	0.87 \pm 0.02	0.84 \pm 0.15

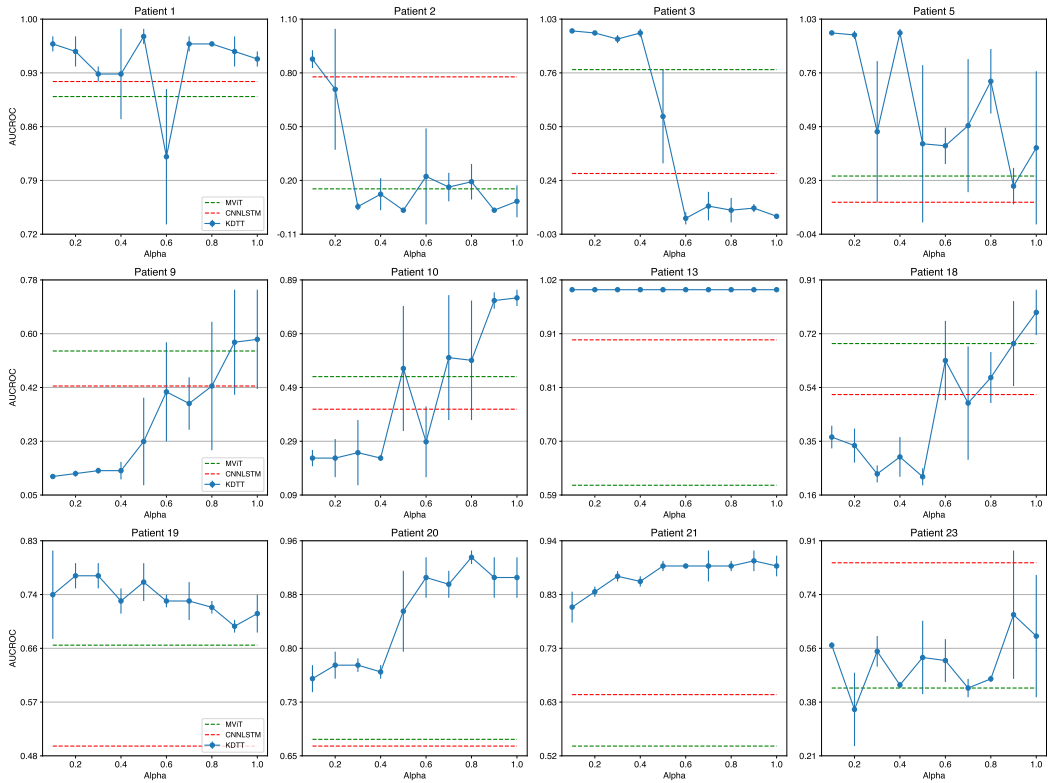


Figure 6: CHBMIT ablation study on alpha. MViT results are represented as a dashed red line, and CNNLSTM results as a dashed green line.

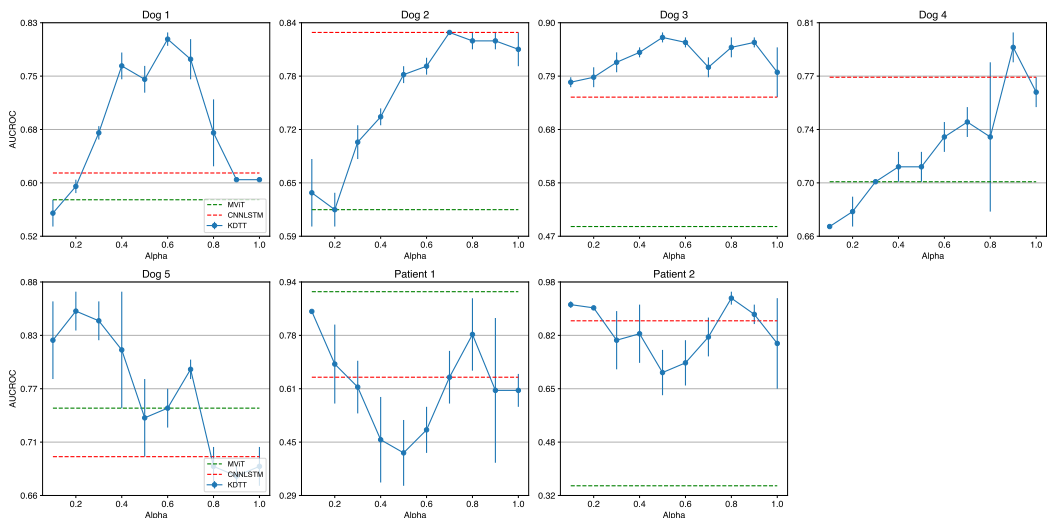


Figure 7: AES ablation study on alpha. MViT results are represented as a dashed red line, and CNNLSTM results as a dashed green line.

Table 2: AES Comparison with SOTA

Patient	MViT			CNNLSTM			FGL		
	FPR	Sensitivity	AUCROC	FPR	Sensitivity	AUCROC	FPR	Sensitivity	AUCROC
Dog 1	0.63 \pm 0.06	0.93 \pm 0.05	0.57 \pm 0.00	0.62 \pm 0.02	1.00 \pm 0.00	0.61 \pm 0.01	0.37 \pm 0.05	0.99 \pm 0.01	0.81 \pm 0.01
Dog 2	0.22 \pm 0.07	0.48 \pm 0.04	0.62 \pm 0.01	0.34 \pm 0.03	0.93 \pm 0.03	0.83 \pm 0.00	0.40 \pm 0.02	0.93 \pm 0.01	0.83 \pm 0.00
Dog 3	0.82 \pm 0.16	0.87 \pm 0.17	0.49 \pm 0.02	0.35 \pm 0.17	0.73 \pm 0.05	0.75 \pm 0.07	0.20 \pm 0.08	0.71 \pm 0.07	0.87 \pm 0.01
Dog 4	0.36 \pm 0.08	0.66 \pm 0.08	0.70 \pm 0.02	0.35 \pm 0.05	0.83 \pm 0.05	0.77 \pm 0.01	0.35 \pm 0.02	0.87 \pm 0.02	0.79 \pm 0.01
Dog 5	0.37 \pm 0.04	0.93 \pm 0.02	0.75 \pm 0.02	0.47 \pm 0.03	0.97 \pm 0.01	0.70 \pm 0.01	0.27 \pm 0.07	0.88 \pm 0.00	0.85 \pm 0.02
Human 1	0.20 \pm 0.07	0.89 \pm 0.03	0.91 \pm 0.04	0.51 \pm 0.16	0.91 \pm 0.09	0.65 \pm 0.17	0.28 \pm 0.01	0.96 \pm 0.02	0.85 \pm 0.00
Human 2	0.98 \pm 0.00	1.00 \pm 0.00	0.35 \pm 0.01	0.21 \pm 0.08	0.82 \pm 0.10	0.86 \pm 0.07	0.28 \pm 0.13	0.90 \pm 0.06	0.93 \pm 0.02
AVG	0.51 \pm 0.28	0.82 \pm 0.16	0.63 \pm 0.15	0.40 \pm 0.12	0.88 \pm 0.08	0.78 \pm 0.06	0.30 \pm 0.02	0.89 \pm 0.01	0.85 \pm 0.01

B Mackey Glass Experiments

B.1 The Mackey Glass Equation

The Mackey-Glass (MG) equation is a delay differential equation used to model chaotic time-series data. It is defined as follows:

$$\frac{dP(t)}{dt} = \frac{\beta_0 \theta^n P(t - \tau)}{\theta^n + P(t - \tau)^n} - \gamma P(t) \quad (8)$$

where:

- $P(t)$: The state variable at time t .
- τ : The time delay parameter.
- β_0 : The growth rate parameter.
- θ : The scaling parameter.
- n : The exponent controlling the nonlinearity.
- γ : The decay rate.

For our experiments, we used the following parameter values:

- $\tau = 17$
- Initial condition $P(0) = 0.9$
- $n = 10$
- $\beta_0 = 0.2$
- $\gamma = 0.1$
- Time step size $dt = 1.0$

B.2 Mackey Glass Dataset Results

C FGL and Predictive Coding

To connect FGL to predictive coding, we review the mathematical intuition behind this theory, as explored in prior work [18, 3]. Using the common mathematical formalisms from these publications, we summarize the relevant concepts in this Appendix to establish a link between predictive processing and FGL. Predictive coding networks can be defined as ensembles of units that compute the posterior probabilities of environmental states $p(v|u)$ based on a top-down prior $p(v)$ and a bottom-up likelihood $p(u|v)$. Assuming Gaussian distributions for these terms, Bayes' theorem allows this computation to be expressed as:

$$p(v|u) = \frac{p(v)p(u|v)}{p(u)} = \frac{\frac{1}{\sqrt{2\pi\Sigma_p}} \exp\left(-\frac{(v-v_p)^2}{2\Sigma_p}\right) \frac{1}{\sqrt{2\pi\Sigma_u}} \exp\left(-\frac{(u-g(v))^2}{2\Sigma_u}\right)}{\int p(v)p(u|v), dv}. \quad (9)$$

Here, v represents a scalar value of the environment, characterized by v_p and Σ_p , the mean and variance of its Gaussian distribution, respectively. Similarly, $p(u|v)$ represents the likelihood, where the scalar u is modeled as the output of an activation function $g(v)$ (e.g., the reflection of light from a surface) with variance Σ_u .

Table 3: FGL Results on Mackey Glass

Horizon	Bins = 25			Bins = 50		
	Baseline	$\alpha = 0.5$	$\alpha = 0.0$	Baseline	$\alpha = 0.5$	$\alpha = 0.0$
2	12.02	9.58	11.14	74.61	50.58	41.79
3	32.02	14.46	11.67	78.48	61.56	55.64
4	60.55	24.98	15.75	259.18	87.35	69.11
5	43.34	37.08	20.18	259.18	111.23	92.00
6	60.55	57.82	43.34	259.18	161.04	105.86
7	60.55	60.55	34.14	259.18	178.96	141.67
8	60.79	34.24	34.24	260.21	260.21	141.98
9	60.79	60.79	32.60	260.21	260.21	141.98
10	60.79	60.79	39.14	260.21	204.12	149.63
11	60.79	61.03	32.63	261.26	261.26	142.23
12	43.67	44.91	32.63	261.26	142.23	146.45
13	58.07	61.03	33.14	190.89	261.26	140.49
14	59.96	61.03	34.31	261.26	261.26	150.04
15	60.22	61.03	34.31	261.26	261.26	150.04
Avg	52.86	45.89	28.33	230.90	185.92	118.48

The denominator in Equation 9 serves as a normalization term that is computationally intractable for biological neural networks due to the need to integrate over all possible combinations of $p(v)$ and $p(u|v)$. One possible simplification is maximum likelihood estimation (MLE), which identifies the value of v that maximizes $p(v|u)$. This value, denoted as Φ , effectively replaces $p(v)$ in an MLE framework. Since the denominator is absent from the left-hand side of Equation 9 under MLE, we can instead focus on the numerator and express its logarithm, F , as:

$$F = \ln(p(\Phi)p(u|\Phi)) = \ln p(\Phi) + \ln p(u|\Phi). \quad (10)$$

We thus derive:

$$\begin{aligned}
 F &= \ln p(\Phi) + \ln p(u|\Phi) \\
 &= \ln \left(\frac{1}{\sqrt{2\pi\Sigma_p}} \exp -\frac{(\Phi - v_p)^2}{2\Sigma_p} \right) + \ln \left(\frac{1}{\sqrt{2\pi\Sigma_u}} \exp -\frac{(u - g(\Phi))^2}{2\Sigma_u} \right) \\
 &= \ln \left(\frac{1}{\sqrt{2\pi\Sigma_p}} \right) + \ln \left(\exp -\frac{(\Phi - v_p)^2}{2\Sigma_p} \right) + \ln \left(\frac{1}{\sqrt{2\pi\Sigma_u}} \right) + \ln \left(\exp -\frac{(u - g(\Phi))^2}{2\Sigma_u} \right) \quad (11) \\
 &= \ln \left(\frac{1}{\sqrt{2\pi}} \right) - \frac{1}{2} \ln \Sigma_p - \frac{(\Phi - v_p)^2}{2\Sigma_p} + \ln \left(\frac{1}{\sqrt{2\pi}} \right) - \frac{1}{2} \ln \Sigma_u - \frac{(u - g(\Phi))^2}{2\Sigma_u} \\
 &= \frac{1}{2} \left(-\ln \Sigma_p - \frac{(\Phi - v_p)^2}{\Sigma_p} - \ln \Sigma_u - \frac{(u - g(\Phi))^2}{\Sigma_u} \right) + C
 \end{aligned}$$

Where C is a constant combining terms that do not depend on Φ .

To determine the maximum likelihood estimate, we compute the derivative of F with respect to the surrogate value Φ :

$$\begin{aligned}
 \frac{\delta F}{\delta \Phi} &= \frac{1}{2} \left(\frac{\delta}{\delta \Phi} \left(-\frac{(u - g(\Phi))^2}{\Sigma_u} \right) + \frac{\delta}{\delta \Phi} \left(-\frac{(\Phi - v_p)^2}{\Sigma_p} \right) + \frac{\delta}{\delta \Phi} (-\ln \Sigma_u) + \frac{\delta}{\delta \Phi} (-\ln \Sigma_p) + \frac{\delta}{\delta \Phi} C \right) \\
 &= \frac{1}{2} \left(\left(-\frac{1}{\Sigma_u} \frac{\delta}{\delta \Phi} (u - g(\Phi))^2 \right) + \left(-\frac{1}{\Sigma_p} \frac{\delta}{\delta \Phi} (\Phi - v_p)^2 \right) \right) \quad (12)
 \end{aligned}$$

Applying the power rule $(f(x)^n)' = nf(x)^{n-1}f'(x)$:

$$\begin{aligned}
\frac{\delta F}{\delta \Phi} &= \frac{1}{2} \left(\left(-\frac{1}{\Sigma_u} 2(u - g(\Phi)) \frac{\delta}{\delta \Phi} (u - g(\Phi)) \right) + \left(-\frac{1}{\Sigma_p} 2(\Phi - v_p) \frac{\delta}{\delta \Phi} (\Phi - v_p) \right) \right) \\
&= \frac{1}{2} \left(\left(-\frac{1}{\Sigma_u} 2(u - g(\Phi)) \left(\frac{\delta}{\delta \Phi} u - \frac{\delta}{\delta \Phi} g(\Phi) \right) \right) + \left(-\frac{1}{\Sigma_p} 2(\Phi - v_p) \left(\frac{\delta}{\delta \Phi} \Phi - \frac{\delta}{\delta \Phi} v_p \right) \right) \right) \\
&= \frac{1}{2} \left(\left(-\frac{1}{\Sigma_u} 2(u - g(\Phi))(-g'(\Phi)) \right) + \left(-\frac{1}{\Sigma_p} 2(\Phi - v_p) \right) \right) \\
&= \left(\frac{1}{\Sigma_u} (u - g(\Phi))(g'(\Phi)) \right) + \left(-\frac{1}{\Sigma_p} (\Phi - v_p) \right) \\
&= \frac{(u - g(\Phi))}{\Sigma_u} g'(\Phi) + \frac{(v_p - \Phi)}{\Sigma_p}
\end{aligned} \tag{13}$$

For simplicity, we rewrite the terms as:

$$\begin{aligned}
\epsilon_p &= \frac{(v_p - \Phi)}{\Sigma_p} \\
\epsilon_u &= \frac{(u - g(\Phi))}{\Sigma_u},
\end{aligned} \tag{14}$$

where ϵ_p represents the prediction error on the causes, and ϵ_u represents the prediction error on the states [7]. Using these terms, the derivative of F with respect to Φ becomes:

$$\frac{\delta F}{\delta \Phi} = \epsilon_u g'(\Phi) + \epsilon_p \tag{15}$$

This gradient can be reformulated as a learning rule:

$$\dot{\Phi} = \epsilon_u g'(\Phi) - \epsilon_p \tag{16}$$

Conceptually, ϵ_p quantifies the prediction error on the causes, capturing the difference between the inferred value (Φ) and the model's prior expectation (v_p) [18]. In contrast, ϵ_u measures the prediction error on the states, reflecting the discrepancy between the observed value (u) and the predicted value ($g(\Phi)$). Simply put, ϵ_p corresponds to errors at higher-level representations, while ϵ_u pertains to raw differences between inferred and actual sensory inputs.

The function F , referred to as the variational free energy, serves as a key metric in predictive coding frameworks. While a detailed discussion is beyond the scope of this appendix, F intuitively relates to information-theoretic concepts, particularly as a lower bound on the model's surprise or uncertainty [7].

In predictive coding, one of the goals of a model is to maximize prediction efficiency and thus minimize both sources of prediction errors. At their minimal values, these errors converge to stable points, ϵ_p and ϵ_u , defined as:

$$\begin{aligned}
\epsilon_p &= \frac{\Phi - v_p}{\Sigma_p} \\
\Sigma_p \epsilon_p &= \Phi - v_p \\
\Phi - v_p - \Sigma_p \epsilon_p &= 0
\end{aligned} \tag{17}$$

$$\begin{aligned}
\epsilon_u &= \frac{u - g(\Phi)}{\Sigma_u} \\
\Sigma_u \epsilon_u &= u - g(\Phi) \\
u - g(\Phi) - \Sigma_u \epsilon_u &= 0
\end{aligned} \tag{18}$$

The dynamics of a system aiming to minimize prediction errors and infer the most likely value of Φ under a MLE approach can then be described as:

$$\begin{aligned}
\dot{\epsilon}_p &= \Phi - v_p - \Sigma_p \epsilon_p \\
\dot{\epsilon}_u &= u - g(\Phi) - \Sigma_u \epsilon_u
\end{aligned} \tag{19}$$

This establishes an intuitive relationship between predictive coding and FGL. In predictive coding, the uncertainties Σ_p and Σ_u parameterize the model. Under an MLE approach, these parameters converge to the most likely value of the inputs, effectively discarding distributional information and reducing the computation to point estimates. While this simplification is efficient, it is inherently incompatible with FGL as presented, where the preservation of distributional richness is critical to leveraging temporal variance and uncertainty effectively.

An alternative to the MLE approach is the use of a “surrogate” distribution via variational inference [20]. Variational inference bypasses the computational intractability of normalization terms (Equation 9) and complex input distributions by introducing a new distribution $q(v)$, which has a standard form characterized by its mean and variance.

In the context of FGL, the student and teacher networks can be more accurately defined within a Bayesian framework. Here, the teacher model acts as a well-posed surrogate $T \approx q(v)$, while the student model is treated as a prior, $S = p(v)$. This framing allows the teacher model to serve as a surrogate representation to guide the student model, effectively approximating the posterior $p(v|u)$ with $q(v)$.

The shift from MLE to variational inference involves minimizing the divergence between the surrogate distribution $q(v)$ and the true posterior $p(v|u)$. This divergence is quantified using the Kullback-Leibler (KL) divergence:

$$KL(q(v), p(v|u)) = \int q(v) \ln \frac{q(v)}{p(v|u)} dv \quad (20)$$

While the KL divergence provides a useful metric, it is implausible for a biological network to directly measure this difference due to the same issue of computational intractability of $p(v|u)$ that led to the use of MLE:

$$p(v|u) = \frac{p(u, v)}{p(u)} = \frac{p(u, v)}{\int p(v)p(u|v)dv} \quad (21)$$

Expanding the KL divergence using the above expression, we have:

$$\begin{aligned} KL(q(v), p(v|u)) &= \int q(v) \ln \frac{q(v)}{p(v|u)} dv \\ &= \int q(v) \ln \frac{q(v)p(u)}{p(u, v)} dv \\ &= \int q(v) \ln \frac{q(v)}{p(u, v)} dv + \int q(v) \ln p(u) dv \end{aligned} \quad (22)$$

Since the surrogate $q(v)$ is a valid probability distribution that integrates to 1, the second term simplifies to $\ln p(u)$, yielding:

$$KL(q(v), p(v|u)) = \int q(v) \ln \frac{q(v)}{p(u, v)} dv + \ln p(u) \quad (23)$$

We define the first term as the variational free energy F , which avoids the need for computing the normalization term and as such, the student’s prior distribution becomes computationally tractable:

$$\begin{aligned} F &= \int q(v) \ln \frac{q(v)}{p(u, v)} dv \\ KL(q(v), p(v|u)) &= F + \ln p(u) \end{aligned} \quad (24)$$

since F depends on the surrogate distribution $q(v)$, the parameters which minimize the distance between the surrogate $q(v)$ and the teacher’s posterior $p(v|u)$, are identical to those which maximize F , which in turn negates the computation of the normalization term. Substituting F , we obtain:

$$\ln p(u) = -F + KL(q(v), p(v|u)) \quad (25)$$

The term $\ln p(u)$, derived above, represents the “surprise” associated with the student’s estimate $p(u)$ of the actual value v , and is directly linked to the uncertainty of the student model. Since the KL divergence is strictly non-negative, F acts as a lower bound for the surprise $\ln p(u)$. Consequently, maximizing F corresponds to minimizing surprise or uncertainty of the student $\ln p(u)$, improving the surrogate approximation $q(v)$, and by extension, optimizing the student model with respect to the teacher in the context of FGL.

This concept of surprise is particularly valuable for updating uncertainty parameters within a network performing predictive computations, where $\ln p(u)$ can be written as:

$$\begin{aligned}
\ln p(u) &= F + KL(q(v), p(v|u)) \\
&= \frac{1}{2} \left[-\ln \Sigma_p - \frac{(\Phi - v_p)^2}{\Sigma_p} - \ln \Sigma_u - \frac{(u - g(\Phi))^2}{\Sigma_u} \right] + C + KL(q(v), p(v|u))
\end{aligned} \tag{26}$$

Since the KL divergence is strictly non-negative, it can be absorbed into the constant C for simplicity, ensuring the expression focuses on terms directly impacting the uncertainty parameters.

Starting from this definition, we can now derive F to optimize v_p :

$$\begin{aligned}
\frac{\delta F}{\delta v_p} &= \frac{1}{2} \left(\frac{\delta}{\delta v_p} \left(-\frac{(\Phi - v_p)^2}{\Sigma_p} \right) + \frac{\delta}{\delta v_p} \left(-\frac{(u - g(\Phi))^2}{\Sigma_u} \right) + \frac{\delta}{\delta v_p} (-\ln \Sigma_u) + \frac{\delta}{\delta v_p} (-\ln \Sigma_p) \right) + \frac{\delta}{\delta v_p} C \\
&= \frac{1}{2} \left(\frac{\delta}{\delta v_p} \left(-\frac{(\Phi - v_p)^2}{\Sigma_p} \right) \right) \\
&= \frac{1}{2} \left(\frac{1}{-\Sigma_p} \frac{\delta}{\delta v_p} (\Phi - v_p)^2 \right) \\
&= \frac{1}{-\Sigma_p} (\Phi - v_p) \frac{\delta}{\delta v_p} (\Phi - v_p) \\
&= \frac{1}{-\Sigma_p} (\Phi - v_p) \left(\frac{\delta}{\delta v_p} \Phi - \frac{\delta}{\delta v_p} v_p \right) \\
&= \frac{\Phi - v_p}{\Sigma_p}
\end{aligned} \tag{27}$$

The same can be done for Σ_p :

$$\begin{aligned}
\frac{\delta F}{\delta \Sigma_p} &= \frac{1}{2} \left(\frac{\delta}{\delta \Sigma_p} \left(-\frac{(\Phi - v_p)^2}{\Sigma_p} \right) + \frac{\delta}{\delta \Sigma_p} \left(-\frac{(u - g(\Phi))^2}{\Sigma_u} \right) + \frac{\delta}{\delta \Sigma_p} (-\ln \Sigma_u) + \frac{\delta}{\delta \Sigma_p} (-\ln \Sigma_p) \right) + \frac{\delta}{\delta \Sigma_p} C \\
&= \frac{1}{2} \left(-\frac{\delta}{\delta \Sigma_p} \ln \Sigma_p + \left(-(\Phi - v_p)^2 \frac{\delta}{\delta \Sigma_p} \frac{1}{\Sigma_p} \right) \right) \\
&= \frac{1}{2} \left(-\frac{1}{\Sigma_p} + \left((\Phi - v_p)^2 \frac{\delta \Sigma_p}{\Sigma_p^2} \right) \right) \\
&= \frac{1}{2} \left((\Phi - v_p)^2 \frac{\delta \Sigma_p}{\Sigma_p^2} - \frac{1}{\Sigma_p} \right) \\
&= \frac{1}{2} \left(\frac{(\Phi - v_p)^2}{\Sigma_p^2} - \frac{1}{\Sigma_p} \right)
\end{aligned} \tag{28}$$

Likewise, for Σ_u :

$$\begin{aligned}
\frac{\delta F}{\delta \Sigma_u} &= \frac{1}{2} \left(\frac{\delta}{\delta \Sigma_u} \left(-\frac{(\Phi - v_p)^2}{\Sigma_p} \right) + \frac{\delta}{\delta \Sigma_u} \left(-\frac{(u - g(\Phi))^2}{\Sigma_u} \right) + \frac{\delta}{\delta \Sigma_u} (-\ln \Sigma_u) + \frac{\delta}{\delta \Sigma_u} (-\ln \Sigma_p) \right) + \frac{\delta}{\delta \Sigma_u} C \\
&= \frac{1}{2} \left(\frac{\delta}{\delta \Sigma_u} \left(-\frac{(u - g(\Phi))^2}{\Sigma_u} \right) - \frac{\delta}{\delta \Sigma_u} \ln \Sigma_u \right) \\
&= \frac{1}{2} \left(-(u - g(\Phi))^2 \frac{\delta}{\delta \Sigma_u} \frac{1}{\Sigma_u} - \frac{\delta}{\delta \Sigma_u} \ln \Sigma_u \right) \\
&= \frac{1}{2} \left(-(u - g(\Phi))^2 \frac{\delta}{\delta \Sigma_u} \frac{1}{\Sigma_u} - \frac{1}{\Sigma_u} \right) \\
&= \frac{1}{2} \left(\frac{(u - g(\Phi))^2}{\Sigma_u^2} - \frac{1}{\Sigma_u} \right)
\end{aligned} \tag{29}$$

Yielding the learned parameters of a predictive coding network that performs equivalent computation to FGL as:

$$\begin{aligned}
\frac{\delta F}{\delta v_p} &= \frac{\Phi - v_p}{\Sigma_p} = \epsilon_p \\
\frac{\delta F}{\delta \Sigma_p} &= \frac{1}{2} \left(\frac{(\Phi - v_p)^2}{\Sigma_p^2} - \frac{1}{\Sigma_p} \right) = \frac{1}{2} (\epsilon_p^2 - \Sigma_p^{-1}) \\
\frac{\delta F}{\delta \Sigma_u} &= \frac{1}{2} \left(\frac{(u - g(\Phi))^2}{\Sigma_u^2} - \frac{1}{\Sigma_u} \right) = \frac{1}{2} (\epsilon_u^2 - \Sigma_u^{-1})
\end{aligned} \tag{30}$$

While these equations follow scalar notations, Bogacz [3] showed that they can trivially be extended to vector and matrices forms with neurobiologically plausible implementations that are computationally similar to FGL.